Astronomy & Astrophysics

Galaxies within galaxies in the TIMER survey: stellar populations of inner bars are scaled replicas of main bars

Adrian Bittner[1,2], Adriana de Lorenzo-Cáceres[3,4], Dimitri A. Gadotti[1], Patricia Sánchez-Blázquez[5,6],
Justus Neumann[7], Paula Coelho[8], Jesús Falcón-Barroso[3,4], Francesca Fragkoudi[9], Taehyun Kim[10],
Ignacio Martín-Navarro[3,4], Jairo Méndez-Abreu[3,4], Isabel Pérez[11,12], Miguel Querejeta[13], and Glenn van de Ven[14]

[1] European Southern Observatory, Karl-Schwarzschild-Str. 2, 85748 Garching bei München, Germany
   e-mail: adrian.bittner@eso.org
[2] Ludwig-Maximilians-Universität, Professor-Huber-Platz 2, 80539 München, Germany
[3] Instituto de Astrofísica de Canarias, Calle Vía Láctea s/n, 38205 La Laguna, Tenerife, Spain
[4] Departamento de Astrofísica, Universidad de La Laguna, 38200 La Laguna, Tenerife, Spain
[5] Departamento de Física de la Tierra y Astrofísica, Universidad Complutense de Madrid, 28040 Madrid, Spain
[6] Instituto de Física de Partículas y del Cosmos, Universidad Complutense de Madrid, 28040 Madrid, Spain
[7] Institute of Cosmology and Gravitation, University of Portsmouth, Burnaby Road, Portsmouth PO1 3FX, UK
[8] Instituto de Astronomia, Geofísica e Ciências Atmosféricas, Universidade de São Paulo, R. do Matão 1226, 05508-090 São Paulo, Brazil
[9] Max-Planck-Institut für Astrophysik, Karl-Schwarzschild-Str. 1, 85748 Garching bei München, Germany
[10] Department of Astronomy and Atmospheric Sciences, Kyungpook National University, Daegu 702-701, Korea
[11] Departamento de Física Teórica y del Cosmos, Universidad de Granada, Facultad de Ciencias, 18071 Granada, Spain
[12] Instituto Universitario Carlos I de Física Teórica y Computacional, Universidad de Granada, 18071 Granada, Spain
[13] Observatorio Astronómico Nacional, C/Alfonso XII 3, Madrid 28014, Spain
[14] Department of Astrophysics, University of Vienna, Türkenschanzstraße 17, 1180 Wien, Austria

ABSTRACT

Inner bars are frequent structures in the local Universe and thought to substantially influence the nuclear regions of disc galaxies. In this study we explore the structure and dynamics of inner bars by deriving maps and radial profiles of their mean stellar population content and comparing them to previous findings in the context of main bars. To this end, we exploit observations obtained with the integral-field spectrograph MUSE of three double-barred galaxies in the TIMER sample. The results indicate that inner bars can be clearly distinguished based on their stellar population properties alone. More precisely, inner bars show significantly elevated metallicities and depleted [α/Fe] abundances. Although they exhibit slightly younger stellar ages compared to the nuclear disc, the typical age differences are small, except at their outer ends. These ends of the inner bars are clearly younger compared to their inner parts, an effect known from main bars as orbital age separation. In particular, the youngest stars (i.e. those with the lowest radial velocity dispersion) seem to occupy the most elongated orbits along the (inner) bar major axis. We speculate that these distinct ends of bars could be connected to the morphological feature of ansae. Radial profiles of metallicity and [α/Fe] enhancements are flat along the inner bar major axis, but show significantly steeper slopes along the minor axis. This radial mixing in the inner bar is also known from main bars and indicates that inner bars significantly affect the radial distribution of stars. In summary, based on maps and radial profiles of the mean stellar population content and in line with previous TIMER results, inner bars appear to be scaled down versions of the main bars seen in galaxies. This suggests the picture of a 'galaxy within a galaxy', with inner bars in nuclear discs being dynamically equivalent to main bars in main galaxy discs.

Key words. galaxies: structure – galaxies: spiral – galaxies: stellar content – galaxies: groups: individual: NGC 1291 – galaxies: individual: NGC 1433 – galaxies: individual: NGC 5850

1. Introduction

Bars are a frequent structure in disc galaxies and important for their secular evolution (see e.g., Kormendy & Kennicutt 2004; Athanassoula et al. 2005; Barazza et al. 2008; Sheth et al. 2008; Aguerri et al. 2009; Masters et al. 2011; Kraljic et al. 2012; Fragkoudi et al. 2020). But some galaxies indeed host more than only one bar: such double-barred systems have a large-scale bar located in their main discs, while another, smaller bar (which we refer to as inner bar[1] throughout this paper) can be found in their

centres. The first double-barred galaxies were already discovered in the 1970s (NGC 1291; de Vaucouleurs 1974, 1975) and early on these objects were thought to be part of a small group of dynamically peculiar galaxies. However, some studies suggest that 30% of all barred galaxies are actually double-barred systems (see e.g., Erwin & Sparke 2002; Laine et al. 2002; Erwin 2004; Buta et al. 2015), while more recently Hildebrandt et al. (2020) estimate a lower limit for the volume-corrected fraction of double bars of 12% in the CALIFA survey (Sánchez et al. 2012).

Despite the amount of known double-barred galaxies and the important secular processes inner bars might induce (Shlosman et al. 1989, 1990), to date, few studies have explored

---

[1] In the literature inner bars are often also referred to as nuclear bars. We warn the reader that sometimes the term nuclear bar is also used to refer to particularly small bars in single-barred systems.

their stellar population content in detail. The first attempt was made by de Lorenzo-Cáceres et al. (2012) using long-slit observations of the galaxy NGC 357. Their results indicate that the bulge and inner bar have similar stellar population properties, while the main bar is less metal-rich and more [α/Fe] enhanced. Subsequent integral-field spectroscopic observations (de Lorenzo-Cáceres et al. 2013) of four additional galaxies are compatible with these results, but further show that inner bars appear slightly younger than their surroundings. Radial profiles reveal positive age and negative metallicity gradients along both the inner and main bars, while [α/Fe] abundances are flat.

The TIMER project (Time Inference with MUSE in Extragalactic Rings; Gadotti et al. 2019) is a survey focussing on central structures, for instance nuclear discs, nuclear rings, and inner bars, observed in massive, barred disc galaxies in the local Universe. To date, 21 galaxies of the sample have been observed with the Multi-Unit Spectroscopic Explorer (MUSE; Bacon et al. 2010) at the Very Large Telescope. While the main goal of the project is to infer the epoch of bar formation from the star formation histories in the central components, previous TIMER studies also explored the nature of inner bars in greater detail. Méndez-Abreu et al. (2019) investigated the face-on galaxy NGC 1291 and, for the first time, detected kinematic signatures of a box/peanut structure associated with the inner bar in this galaxy. More precisely, bi-symmetric minima of the higher-order moment h_4 of the line-of-sight velocity distribution are observed along the inner bar major axis, which is as expected from numerical simulations and identified in the context of main bars (see e.g., Debattista et al. 2005; Méndez-Abreu et al. 2008, 2014). Similarly, Bittner et al. (2019) observed a correlation between radial velocity and the higher-order moment h_3 in the spatial region of the inner bar of NGC 1433. This correlation is a well-known kinematic signature of main bars, arising from the strongly elongated x_1 orbits within them (Bureau & Athanassoula 2005; Iannuzzi & Athanassoula 2015; Li et al. 2018; Gadotti et al. 2020). Detecting this correlation for an inner bar again suggests that both types of bars are dynamically similar structures. Finally, de Lorenzo-Cáceres et al. (2019) combined multi-component photometric decompositions of NGC 1291 and NGC 5850 with measurements of kinematics and the stellar population content. The results show that nuclear discs and inner bars have similar radii, suggesting that inner bars form via dynamical instabilities in nuclear discs in the same way main bars arise in the main discs of galaxies. In addition, the star formation histories indicate that the inner bars in NGC 5850 and NGC 1291 are at least 4.5 Gyr and 6.5 Gyr old, implying that inner bars are dynamically stable, long-lived structures.

The stellar population properties of main bars have been studied in greater detail. Pérez et al. (2007, 2009) detected large variations of ages and metallicities in bars, with positive, null, and negative metallicity gradients along their major axis. Sánchez-Blázquez et al. (2011) compared the stellar content of bars with that in the main discs of these galaxies, indicating that bars host, on average, older stellar populations with higher metallicities than the galaxy discs. The gradients in both parameters appear flatter along the bar major axis compared to the gradients found in the main disc. Using 128 galaxies from the MaNGA survey (Bundy et al. 2015), Fraser-McKelvie et al. (2019) found that the gradients of age and metallicity along the bar are typically flatter compared to the region outside of the bar but within the bar radius (see also Seidel et al. 2016). Neumann et al. (2020) exploited the high spatial resolution observations of the TIMER survey to explore stellar population gradients not only along the bar major axis, but also perpendicular to it. The results show that the youngest stellar populations in bars are located closest to the bar major axis, suggesting that the youngest stars populate the most elongated orbits.

The large number of morphological features in disc galaxies, especially in their centres, has led astronomers to introduce a variety of nomenclatures for these structures. In this study, we use the term nuclear disc to refer to rotationally supported central discs with typical sizes of a few hundred parsecs that are kinematically distinct from the main galaxy disc. We choose this nomenclature to distinguish nuclear discs from inner and outer discs, as often referred to in the context of disc breaks. The outermost edge of nuclear discs are often distinguished by gaseous and/or star-forming rings. These structures are named nuclear rings, in order to discriminate them from inner rings typically found at the radius of the main bar and outer rings located well outside of the main bar. For the double-barred systems presented here, we use the term inner bar when referring to small-scale bars associated with nuclear discs while large-scale bars found in the main discs of galaxies are simply denoted bar or main bar, as appropriate.

In this paper, we investigate the similarities between the stellar populations of main bars and inner bars by exploiting two-dimensional stellar population maps and radial profiles, based on the high-resolution, integral-field spectroscopic observations of the TIMER survey. We further complement the study of de Lorenzo-Cáceres et al. (2019) by exploring how the stellar population properties vary along and perpendicular to inner bars. In particular, we present for the first time radial profiles of stellar population properties along the inner bar major and minor axis. We then compare these results to those obtained by Neumann et al. (2020) in the context of main bars. Based on these investigations, we explore the dynamical structure of inner bars, argue that main and inner bars appear to be scaled versions of each other, and speculate about the nature of ansae.

This paper is structured as follows: in the next section we summarise observations, data reduction, sample selection, and analysis which are already detailed in previous papers. In Sect. 3 we show our results on the stellar population content of inner bars before discussing them in the context of main bars in Sect. 4. Finally, we summarise our conclusions in Sect. 5.

2. Sample, observations, and data analysis

In this section we briefly summarise our sample of inner bars, the TIMER observations and data reduction, as well as the performed data analysis.

2.1. Double-barred galaxies in TIMER

The TIMER sample is selected from the *Spitzer* Survey of Stellar Structures in Galaxies (S^{4}G, Sheth et al. 2010). Therefore, all galaxies are nearby ($d < 40$ Mpc), bright ($m_B < 15.5$ mag), and large ($D_{25} > 1$ arcmin) objects. In addition, only barred galaxies with central structures, as determined by Buta et al. (2015), stellar masses above $10^{10}\ M_\odot$, and inclinations below 60 deg are included.

Among the 21 TIMER galaxies observed so far, only NGC 1291 and NGC 5850 exhibit prominent inner bars. These inner bars have already been detected in previous studies on the subject (see e.g., Erwin 2004; Buta et al. 2015; de Lorenzo-Cáceres et al. 2008, 2013) and recently investigated within the TIMER survey (de Lorenzo-Cáceres et al. 2019; Méndez-Abreu et al. 2019). In contrast, the presence of an inner bar in the centre of NGC 1433 remains debated: previous photometric studies
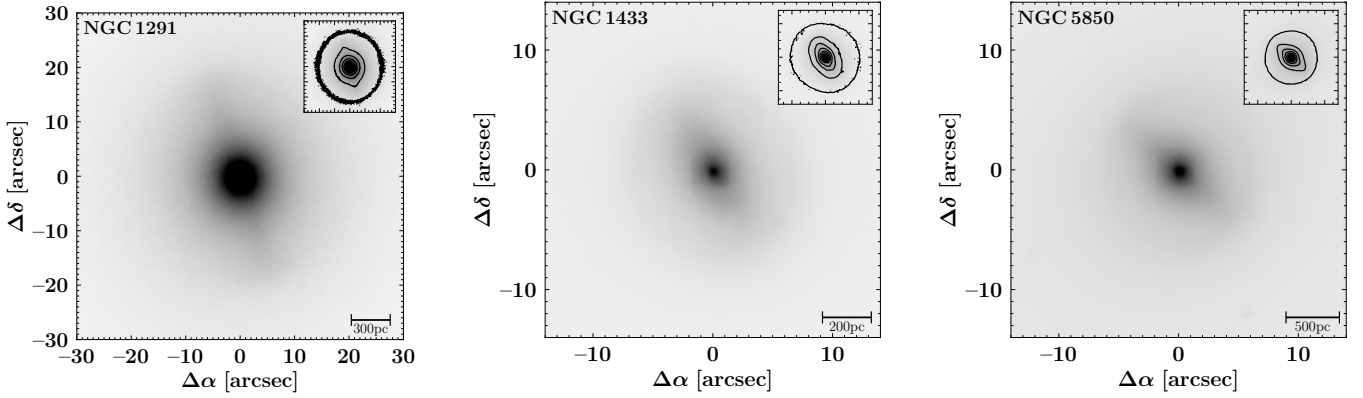
Fig. 1. Photometric *H*-band observations of the inner bars and nuclear discs in NGC 1291, NGC 1433, and NGC 5850, obtained with HAWK-I. The insets show exactly the same field of view as the main images and illustrate the isophotes in the galaxy centres which highlight not only the axisymmetric structure of the nuclear discs but also the significantly elongated inner bars. For the three galaxies the inner bar is clearly distinguishable, in particular also the relatively weak inner bar of NGC 1433 whose existence has been debated. North is up; east is to the left.

Table 1. Overview of some fundamental properties of the sample.

Name	i (deg)	$M_\star$ ($10^{10} M_\odot$)	PA_{gal} (deg)	d (Mpc)	Spatial scale (pc arcsec^{-1})	r_{kin} (kpc)	Source	PA_{ib} (deg)	a_{full} (arcsec)	a_{vis} (arcsec)	b/a
(1)	(2)	(3)	(4)	(5)	(6)	(7)	(8)	(9)	(10)	(11)	(12)
NGC 1291	11	5.8	−8.9	8.6	42	–	HE	18	–	19.3	0.78
							LC	17	29.0	–	0.35
NGC 1433	34	2.0	18.2	10.0	49	0.381	HE	30	–	7.1	0.67
							LC	–	–	–	–
NGC 5850	39	6.0	−26.5	23.1	112	0.796	HE	45	–	7.1	0.72
							LC	48	11.3	–	0.21

Notes. Shown are the inclination *i* of the galaxy disc relative to the plane of the sky in Col. (2), the total stellar mass $M_\star$ in Col. (3), the position angle of the galaxy disc PA_{gal} in Col. (4) (all from S^{4}G; Sheth et al. 2010; Muñoz-Mateos et al. 2013, 2015), the mean redshift-independent distance *d* from the NASA Extragalactic Database (NED, http://ned.ipac.caltech.edu/) in Col. (5), the spatial scale of the observations in Col. (6), and the kinematic radius of the nuclear disc in Col. (7) (Gadotti et al. 2020). Column (8) states the source of the structural components described in the following columns: HE refers to the results from Herrera-Endoqui et al. (2015) while LC designates the multi-component decompositions of de Lorenzo-Cáceres et al. (2019). We refer the reader to Sect. 3.1 for a comparison of the results of both methods. Columns (9)–(12) provide the position angle of the inner bar PA_{ib}, its full semi-major axis a_{full} from photometric decompositions, the inner bar semi-major axis from visual inspections a_{vis}, and the inner bar axial ratio b/a. We note that no kinematic radius could be determined for NGC 1291, due to the face-on orientation of the galaxy. NGC 1433 is not included in the photometric decompositions of de Lorenzo-Cáceres et al. (2019).

(Buta 1986; Jungwiert et al. 1997; Erwin 2004; Buta et al. 2015) show some evidence of an inner bar and Bittner et al. (2019) finds consistent kinematic signatures. However, de Lorenzo-Cáceres et al. (2019) inspected recent *Hubble* Space Telescope images of the galaxy and concluded that NGC 1433 does not host an inner bar. They argue that the presence of a variety of central structures, such as a nuclear ring, nuclear disc, and nuclear spiral arms has led to a misclassification in this galaxy. Moreover, they state that the absence of clear σ-hollows, a kinematic feature typically associated with inner bars, further suggests that this galaxy does not host an inner bar.

In Fig. 1 we present *H*-band observations of the central regions of the three galaxies, recently obtained with the HAWK-I imager (Kissler-Patig et al. 2008) at ESO's Paranal Observatory. These observations were performed employing the Adaptive Optics correction produced by the GRAAL AOF module (Paufique et al. 2010) on UT4, leading to a typical point-spread function of about 0.4 arcsec to 0.5 arcsec. The high-resolution photometric observations not only highlight the structure of the inner bars in NGC 1291 and NGC 5850, but also show the inner bar in NGC 1433 more clearly. Although the inner bar in this galaxy does not appear as prominent as in the two other cases, the isophotes reveal the elongated structure of this inner bar within an almost axisymmetric nuclear disc. In fact, the detection of inner bars with varying strength is not surprising, as main bars also exhibit a large range of structural properties.

In addition, we carefully inspected the inner regions of all other TIMER galaxies using S^{4}G images, our recent HAWK-I photometry, reconstructed intensities from MUSE, and maps of kinematics and stellar population properties (Bittner et al. 2020; Gadotti et al. 2020). Although some studies report inner bar fractions of 30% (e.g., Erwin & Sparke 2002), no other inner bars are detected in the TIMER sample. In fact, the detected number of inner bars in the sample is consistent with more recent estimates of a 12% frequency of double-barred systems (Hildebrandt et al. 2020).

In Table 1 we present an overview about some of the fundamental properties of the three galaxies considered in this study, including inclination, position angle, stellar mass, and distance. All galaxies exhibit clear evidence of a nuclear disc and we show their kinematic radii, defined as the radius at which v/σ within the nuclear disc reaches its maximum (Gadotti et al. 2020).

Finally, we present the basic properties of the inner bars, that is their position angles, radii, and axis ratios, based on the visual inspections of Herrera-Endoqui et al. (2015) and careful multi-component decompositions of de Lorenzo-Cáceres et al. (2019). In fact, these decompositions include 6 different galaxy components and thus highlight how complicated the inner regions of these galaxies are. We discuss the differences in the estimated parameters in Sect. 3.1.

2.2. Observations and data reduction

Exploiting the wide-field mode of the MUSE spectrograph, most TIMER observations were obtained in ESO's period 97 from April to September 2016. The observations use a wavelength range from 4750 Å to 9350 Å at a spectral sampling of 1.25 Å. The field of view covers 1 arcmin^2 with a spatial sampling of 0.2 arcsec at a typical seeing of 0.8 arcsec to 0.9 arcsec. Each observation included approximately 1 h of integration on source. Since all galaxies are larger than the field of view, dedicated sky exposures were obtained.

Following the standard TIMER data reduction procedure, the observations were reduced with version 1.6 of the MUSE data reduction pipeline (Weilbacher et al. 2012, 2020). More specifically, the data are calibrated in flux and wavelength, and bias, flat-fielding, and illumination corrections are applied. Telluric features as well as the sky background are removed, the latter using principal component analysis. Finally, the data is registered astrometrically. A detailed overview of observations and data reduction of the TIMER survey is presented in Gadotti et al. (2019).

2.3. Data analysis

The analysis of the MUSE data is performed within the fully modular software framework of the GIST pipeline[2] (Galaxy IFU Spectroscopy Tool, Bittner et al. 2019). This tool provides extensive capabilities for the analysis of spectroscopic data, facilitating all necessary steps from the read-in and preparation of input data, over its scientific analysis, to the production of publication quality plots. In the following, we only summarise the conducted data analysis while a more detailed description is provided in Bittner et al. (2020).

We use the GIST framework to exploit the adaptive Voronoi tesselation routine of Cappellari & Copin (2003), in order to spatially bin the data to an approximately constant signal-to-noise ratio of 100. This high signal-to-noise ratio is employed to ensure the reliability of the measurement (see Bittner et al. 2020, for an assessment of the influence of the signal-to-noise ratio on the derived population properties).

We adopt the udf-10 parametrisation of Bacon et al. (2017) to model the line-spread function of the MUSE spectra. All template spectra are broadened to this resolution before any fits are performed. We further employ the wavelength range from 4800 Å to 5800 Å in this analysis. This relatively short portion of the MUSE wavelength range is chosen because the red part of the spectra is not optimal for the measurement of stellar population properties. In particular, the lower sensitivity to young stellar populations, residuals from the sky subtraction, as well as absorption lines originating in the interstellar medium would complicate the analysis (see e.g., Gonçalves et al. 2020).

The measurement of the stellar population properties is performed in three separate steps, using the full-spectral fitting approach. Firstly, we employ the pPXF routine (Cappellari & Emsellem 2004; Cappellari 2017) to derive the stellar kinematics, while keeping emission lines masked. A low order multiplicative Legendre polynomial is employed, in order to account for differences in the continuum shape between spectra and templates. Secondly, we apply pyGandALF (Bittner et al. 2019), a new Python implementation of the original GandALF routine (Sarzi et al. 2006; Falcón-Barroso et al. 2006), in order to fit any present emission lines while taking into account the results from the previous stellar kinematics fit. pyGandALF uses a two-component reddening correction instead of corrective Legendre polynomials that accounts for extinction within the emission-line regions as well as for 'screen-like' extinction that affects the entire spectrum. The detection of emission lines is considered significant if the amplitude-to-residual-noise ratio exceeds four. In these cases, the emission line is subtracted from the spectrum, thus obtaining emission-subtracted spectra.

Thirdly, a regularised run of pPXF is performed in order to measure the mean stellar population properties, using the emission-subtracted spectra. In this process, we apply an 8th order multiplicative Legendre polynomial. We further fix the stellar kinematics to those derived with the unregularised run of pPXF in order to avoid degeneracies between metallicity and velocity dispersion (see e.g., Sánchez-Blázquez et al. 2011). In fact, pPXF does not directly derive mean stellar population properties but instead non-parametric star formation histories. This is achieved by assigning weights to the spectral models so that the observed spectra are best reproduced. However, it is not straightforward to obtain a physically meaningful solution, as this is an ill-conditioned inverse problem. Therefore, pPXF applies a regularisation, such that the smoothest solution that is consistent with the data is returned (Press et al. 1992; Cappellari 2017). We determine the regularisation strength following the prescription applied, for instance, by McDermid et al. (2015) and detailed in Bittner et al. (2020).

Throughout the analysis, we use the MILES single stellar population (SSP) models (Vazdekis et al. 2015) as spectral templates. These models use a Kroupa Revised IMF with a slope of 1.30 (Kroupa 2001) and BaSTI isochrones (Pietrinferni et al. 2004, 2006, 2009, 2013). The models cover ages from 0.03 Gyr to 14 Gyr, metallicities from −2.27 dex to 0.40 dex, and [α/Fe] enhancements of 0.00 dex and 0.40 dex at a spectral resolution of 2.51 Å (Falcón-Barroso et al. 2011).

In this study, we derive light-weighted stellar population properties, in order to emphasise differences in the stellar ages. Such light-weighted population properties are obtained by normalising each MILES model by its own mean flux. Average population properties are then calculated from the weight w_i assigned to the model i via

$$\langle t \rangle = \frac{\sum_i w_i \, t_{\mathrm{SSP},i}}{\sum_i w_i} \tag{1}$$

$$\langle [\mathrm{M/H}] \rangle = \frac{\sum_i w_i \, [\mathrm{M/H}]_{\mathrm{SSP},i}}{\sum_i w_i} \tag{2}$$

$$\langle [\alpha/\mathrm{Fe}] \rangle = \frac{\sum_i w_i \, [\alpha/\mathrm{Fe}]_{\mathrm{SSP},i}}{\sum_i w_i} \tag{3}$$

with the ith model having an age of $t_{\mathrm{SSP},i}$, metallicity $[\mathrm{M/H}]_{\mathrm{SSP},i}$, and an [α/Fe] enhancement of $[\alpha/\mathrm{Fe}]_{\mathrm{SSP},i}$.

These [α/Fe] enhancements are an indicator of the longevity of star formation in galaxies. As α-elements are predominantly formed in the fusion processes leading to type II supernovae

---

[2] http://ascl.net/1907.025

while iron is mostly produced in type Ia supernovae (see e.g., Worthey et al. 1992; Weiss et al. 1995), the [α/Fe] abundance gives an estimate of their relative importance. Since the progenitor stars of type II supernovae are massive and short-lived while those of type Ia supernova have long lifetimes, the timescale of star formation in a galaxy is constrained by these [α/Fe] enhancements: High abundances hint towards short and intense star-formation episodes, while low [α/Fe] abundances are a signature of slow but continuous star formation.

3. Results

In the following we present our results on the stellar population content of inner bars. In particular, we present maps of the mean population properties and their radial profiles along and perpendicular to the inner bar major axis. The measurements of the stellar population properties employed in this study are made publicly available[3].

3.1. Mean stellar population properties in inner bars

In Fig. 2 we present light-weighted maps of the mean stellar population properties of NGC 1291, NGC 1433, and NGC 5850, similar to the ones presented in Bittner et al. (2020) but focussed on the spatial region of the inner bar. In all three galaxies, the inner bars are easily distinguishable, based on their mean stellar populations alone, as previously claimed by de Lorenzo-Cáceres et al. (2013). Most strikingly, the inner bars show significantly elevated metallicities and reduced [α/Fe] enhancements. This effect is most pronounced in NGC 1291 and NGC 5850 in which the deviating metallicities and [α/Fe] abundances are clearly confined to the long and thin inner bar. To some degree, the same holds for NGC 1433: while the inner bar in this galaxy appears slightly rounder, this structure is still distinct in the [M/H] and [α/Fe] abundance maps.

In contrast to metallicities and [α/Fe] enhancements, inner bars do not show significantly different mean stellar ages in the largest part of their spatial extent. However, in all cases the ends of the inner bars are associated with relatively younger stellar populations, although these populations can still be very old, especially in the case of NGC 1291. These younger ends of the inner bars are broader perpendicular to the inner bar major axis. Thanks to the superior physical resolution of the observation of NGC 1291 (simply because this galaxy is closer), this effect is again most prominent in this galaxy and in line with the morphological properties of its inner bar (see e.g., Méndez-Abreu et al. 2019; de Lorenzo-Cáceres et al. 2019).

The ends of the inner bars are located close to the outer edge of the nuclear disc, a region that is often highlighted by gaseous nuclear rings (see Bittner et al. 2020, for a discussion of the differences between nuclear discs and nuclear rings). Therefore, the relatively young ends of the inner bar might be affected by recent star formation in the nuclear ring. At least for the galaxies in the present sample this is likely not the case. Maps of the Hα emission-line fluxes which trace HII regions and hence star formation, do not show concentrated emission at the ends of the inner bars (Neumann et al. 2020; Bittner et al. 2020). Moreover, the galaxies in the present sample do not host gaseous (star-forming) nuclear rings that might cause the observed effect of inner bars having young stellar populations at their ends. In addition, star formation that did not proceed very recently and, thus, might not be traceable with the Hα emission-line fluxes anymore

should not result in such spatially well-defined young ends of the inner bars. Due to the short dynamical timescale in these radial regions, the young stellar populations would mix and their signature at the bar ends vanish rapidly.

Further, we overplot the maps of the mean stellar population properties in Fig. 2 with ellipses highlighting the spatial extent of the inner bars, as previously determined based on photometric data from S^{4}G. The black dash-dotted ellipses are based on the visual estimates of the inner bar structural properties from Herrera-Endoqui et al. (2015). While the length of the inner bar major axis coincides well with the appearance of the stellar population maps (in particular considering metallicities and [α/Fe] abundances), the ellipses are in all cases too round. However, this behaviour is expected, as the measurement is performed on integrated light from multiple overlapping galaxy components (see also de Lorenzo-Cáceres et al. 2020). In particular the axisymmetric structure of nuclear discs is expected to bias the inner bar ellipticity towards rounder shapes. In contrast, the black dashed ellipses in Fig. 2 are derived using detailed, multi-component decompositions (de Lorenzo-Cáceres et al. 2019). Such photometric decompositions actually separate the light from the different galaxy components and are, thus, able to better reproduce the elongated shapes of the inner bars observed in the mean population maps. However, the inner bar full radii are larger than the inner bars appear in the maps. This is a result of the fact that the bar ends are faint and contaminations from other components, for instance stars in the main bar and main disc, become significant. In fact, these systematic differences of bar lengths and ellipticities derived via different methods have already been noted in the case of main bars (Gadotti 2008, 2011). Taking into account these differences, in the remainder of this paper we use inner bar lengths from the visual estimates of Herrera-Endoqui et al. (2015) and ellipticities from the multi-component decompositions of de Lorenzo-Cáceres et al. (2019) in order to highlight the spatial extent of inner bars (solid ellipses in Fig. 2). This combination of photometric estimates traces the appearance of inner bars in the stellar population maps excellently. Nonetheless, the differences between the measurement methods again show how complicated the central regions of these galaxies are due to multiple, overlapping galaxy components.

The stellar population properties of the inner bar of NGC 5850 were first studied by de Lorenzo-Cáceres et al. (2013), based on observations with the SAURON spectrograph (Bacon et al. 2001). To this end, they derived single stellar population equivalent population properties from the measurement of line strength indices at a signal-to-noise level of 60. In agreement with the results presented here, they find that the inner bar of NGC 5850 has systematically higher metallicities compared to its immediate surroundings. However, in their study the inner bar shows only a weak indication of systematically lower [α/Fe] abundances. We speculate that this is a result of the different measurement methods, that is the use of line strength indices to infer an [Mg/Fe] overabundance, as compared to the use of full spectral fitting to derive [α/Fe] enhancements here.

In a previous TIMER publication, de Lorenzo-Cáceres et al. (2019) investigated various possible formation scenarios for inner bars based on an independent analysis. In their study, they choose to spatially bin the MUSE data to a signal-to-noise ratio of 40 (as compared to a signal-to-noise of 100 used here), model and remove emission lines with GandALF, and fit ages and metallicities with STECMAP (Ocvirk et al. 2006a,b). [α/Fe] enhancements are estimated based on a set of line-strength indices. While their analysis uses different techniques and routines, the stellar population properties agree qualitatively well with the
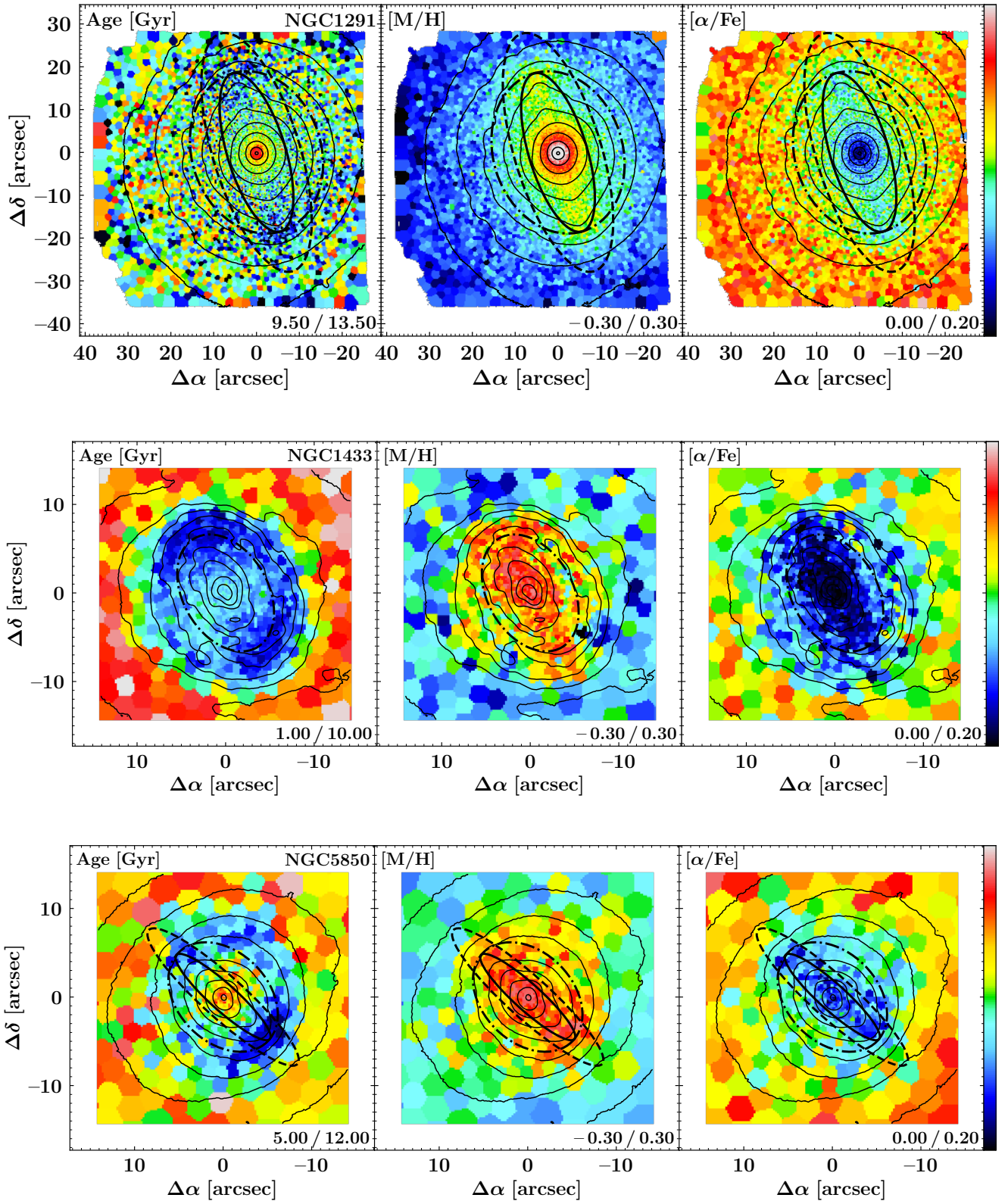
---

[3] https://www.muse-timer.org

Fig. 2. Maps of light-weighted, mean stellar population properties of NGC 1291 (*upper panels*), NGC 1433 (*central panels*), and NGC 5850 (*lower panels*), focussed on the spatial region of the inner bar (see Bittner et al. 2020, for maps showing the entire MUSE field of view). Each set of panels displays age, [M/H], and [α/Fe] enhancements and the limits of the respective colour bar are stated in the lower-right corner of each panel. The dash-dotted ellipses display the approximate extent of the inner bars according to the visual measurements of Herrera-Endoqui et al. (2015), while dashed ellipses show the results from the multi-component decompositions of de Lorenzo-Cáceres et al. (2019). Solid ellipses combine the inner bar lengths from Herrera-Endoqui et al. (2015) with the ellipticities of de Lorenzo-Cáceres et al. (2019) and trace the appearance of the inner bars excellently. NGC 1433 is not included in the photometric decompositions of de Lorenzo-Cáceres et al. (2019), hence only a dash-dotted ellipse is displayed. Based on the reconstructed intensities from the MUSE cube, we display isophotes in steps of 0.5 mag. North is up; east is to the left.
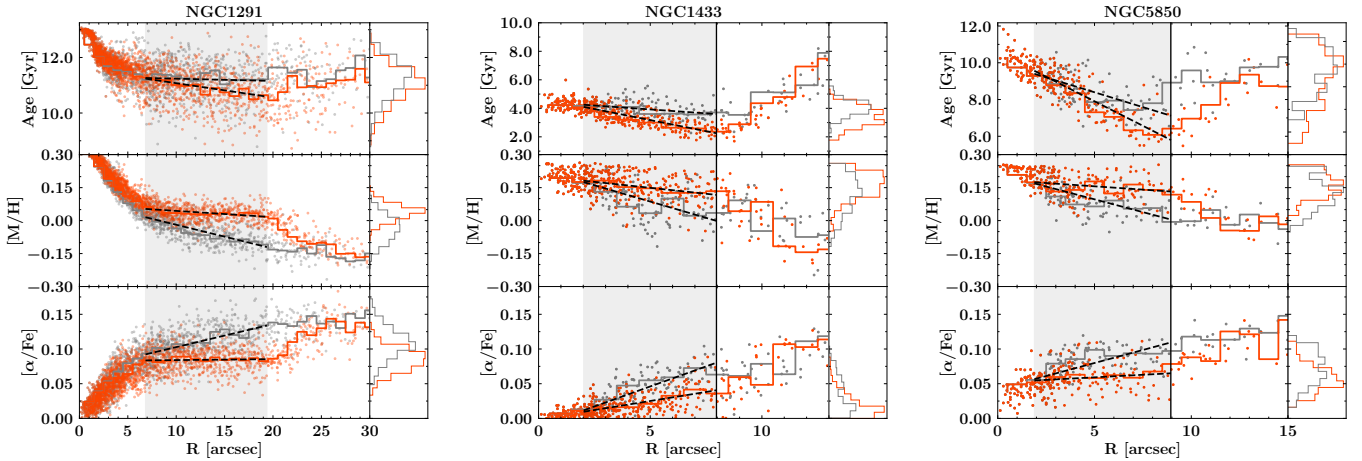
Fig. 3. Radial profiles of ages (*upper panels*), metallicities (*central panels*), and [α/Fe] abundances (*lower panels*) as a function of the galactocentric radius. The profiles have been deprojected using inclinations and position angles derived in S⁴G, as presented in Table 1. Profiles along and perpendicular to the major axis of the inner bar are displayed in orange and grey, respectively. To better highlight the radial trends, we also plot the median population properties in bins of 1 arcsec (solid lines). Shaded regions highlight the radial range of the inner bars, i.e. for NGC 1291 and NGC 5850 the range between the inner bar minor and major axis radius, calculated using the inner bar radius from Herrera-Endoqui et al. (2015) and ellipticity from de Lorenzo-Cáceres et al. (2019). Since the inner bar properties of NGC 1433 are not constrained by photometric studies, we highlight the radial range between 2 arcsec (in order to approximately exclude the range in which both the minor and major axis profiles probe the inner bar) and the kinematic radius of the nuclear disc from Gadotti et al. (2020). Dashed lines show linear fits to the population profiles within the radial range of the inner bar. The histograms on the right display the distribution of stellar population properties in the inner bar major and minor axis, again within the radial range of the inner bar. The vertical solid lines represent the kinematic radii of the nuclear discs (Gadotti et al. 2020). We note that for NGC 1291 no kinematic radius could be determined, due to the face-on orientation of the galaxy.

Table 2. Overview of radial slopes and mean stellar population properties in the inner bars.

		Age-slope	[M/H]-slope	[α/Fe]-slope	$\langle$Age$\rangle$	$\langle$[M/H]$\rangle$	$\langle$[α/Fe]$\rangle$
NGC 1291	MA	$(-5.15 \pm 0.69) \times 10^{-2}$	$(-2.8 \pm 0.4) \times 10^{-3}$	$(1 \pm 1) \times 10^{-4}$	10.97	0.04	0.08
	MI	$(-8.1 \pm 8.4) \times 10^{-3}$	$(-1.08 \pm 0.05) \times 10^{-2}$	$(3.3 \pm 0.3) \times 10^{-3}$	11.22	−0.04	0.11
NGC 1433	MA	$(-3.11 \pm 0.16) \times 10^{-1}$	$(-1.1 \pm 0.2) \times 10^{-2}$	$(5.2 \pm 0.5) \times 10^{-3}$	3.43	0.16	0.02
	MI	$(-1.10 \pm 0.24) \times 10^{-1}$	$(-2.97 \pm 0.32) \times 10^{-2}$	$(11.5 \pm 0.7) \times 10^{-3}$	4.03	0.12	0.03
NGC 5850	MA	$(-5.338 \pm 0.297) \times 10^{-1}$	$(-6.0 \pm 2.2) \times 10^{-3}$	$(1.5 \pm 0.8) \times 10^{-3}$	8.28	0.16	0.06
	MI	$(-3.236 \pm 0.339) \times 10^{-1}$	$(-2.33 \pm 0.25) \times 10^{-2}$	$(7.5 \pm 0.9) \times 10^{-3}$	8.73	0.12	0.07

Notes. Slopes of the linear fits to the stellar population properties along the inner bar major (MA) and minor axis (MI) in the radial range of the inner bar (in units of Gyr arcsec^{-1} and dex arcsec^{-1}). We further provide the mean stellar population properties in this radial range (in units of Gyr and dex).

results presented here, in particular when considering that pPXF returns systematically higher stellar ages than STECMAP (see Bittner et al. 2020). In fact, the stellar population properties of the inner bar of NGC 5850 agree well with the ones presented here. de Lorenzo-Cáceres et al. (2019) conclude that the middle part of the inner bar in NGC 1291 is slightly older compared to its surroundings, while in the present study no age difference is detected in this part of the inner bar. In fact, as STECMAP returns systematically younger stellar ages, subtle differences in age are emphasised that remain unnoticed with pPXF, especially at the observed ages of >10 Gyr at which it is challenging to reliably distinguish stellar ages. Nonetheless, a careful visual comparison reveals that the young ends of the inner bar appear to be already detected by de Lorenzo-Cáceres et al. (2019). Hence, the stellar population properties estimated in the two studies are consistent.

3.2. Profiles along the inner bar major and minor axis

In Fig. 3 we plot light-weighted stellar ages, metallicities, and [α/Fe] abundances as a function of the deprojected galactocentric radius. These profiles are calculated based on pseudo-slits crossing the galaxy centre and being oriented along and perpendicular to the major axis of the inner bar, according to the position angles presented in Table 1. We include all spatial bins within a pseudo-slit with a width of 2 arcsec but check that using different widths, for instance 1 arcsec or 4 arcsec, do not alter the obtained profiles qualitatively.

Naturally, the radial population profiles clearly corroborate the findings from the stellar population maps. In Table 2 we provide an overview of the mean stellar population properties measured along and perpendicular to the inner bar major axis. Average differences vary between galaxies, but indicate that inner bars are systematically more metal-rich and less [α/Fe] enriched (see Table 2). We note that the differences between the major and minor axis depend on the radius and, hence, the typical differences at the inner bar radius are significantly larger than the average differences in the radial region of the inner bar. Considering stellar ages, inner bars seem to be slightly younger, although typical age differences are relatively small. In line with our findings from the population maps, the largest age differences
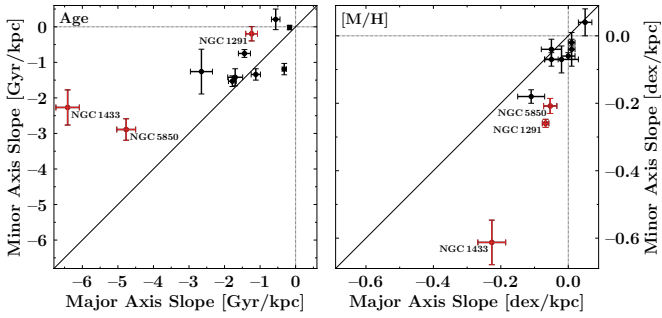
Fig. 4. Comparison of the age (*left-hand panel*) and metallicity (*right-hand panel*) slopes measured along the major and minor axis of the inner bars in this study (red data) and the main bars from Neumann et al. (2020, black data).

are found close to or just outside of the inner bar radius, reaching maximum age differences of 2 Gyr for NGC 5850, and between 1 Gyr to 2 Gyr in the case of NGC 1433. These absolute age differences at the ends of the inner bar remain below 1 Gyr only for NGC 1291. In fact, the observed age differences somewhat depend on the absolute values of stellar age. Distinguishing the ages of stellar populations at old ages, for instance in the case of the >10 Gyr populations in NGC 1291, is very difficult, possibly indicating that in this case the age differences are not significant.

Another interesting aspect are the slopes of the stellar population profiles inside the inner bars, especially when considering metallicity and [α/Fe] abundances. The [M/H] and [α/Fe] profiles along the inner bar major axis of NGC 1291 are steeply decreasing/increasing from the centre, an effect that is most likely due to the small kinematically hot spheroid in this galaxy with an effective radius of 9.9 arcsec (de Lorenzo-Cáceres et al. 2019). However, the profiles are remarkably flat in the radial range occupied by the inner bar (shaded area in Fig. 3). A prominent break in the profiles is evident at the inner bar radius where [M/H] and [α/Fe] steeply decrease/increase and converge to the lower/higher values typically observed outside of the nuclear disc. In contrast, the slopes along the inner bar minor axis differ significantly from those along the inner bar major axis. In fact, the minor axis profiles smoothly connect the steep slopes in the innermost region to the values at large radii, showing a larger/lower slope. The inner bar of NGC 5850 follows exactly the same trends, however, the effect is less prominent for NGC 1433. The latter is not surprising, as the inner bar in this galaxy is somewhat weaker and less elongated. Interestingly, such flat radial profiles are not evident when considering the stellar ages of any galaxy in the sample. Instead, the observed stellar ages are continuously decreasing both along and perpendicular to the inner bar. In all three galaxies of the present sample, the stellar ages are decreasing more strongly along the inner bar major axis than perpendicular to it.

In order to better quantify these findings, we fitted ages, metallicities, and [α/Fe] abundances of the three galaxies in the radial range of the inner bar (shaded area in Fig. 3). For NGC 1291 and NGC 5850, this is the radial range between the inner bar minor and major axis radius, as determined from the measurements of de Lorenzo-Cáceres et al. (2019) and Herrera-Endoqui et al. (2015). Equivalently, for NGC 1433 we chose the radial range between 2 arcsec (in order to exclude the radial region where both major and minor axis still probe the inner bar) and the kinematic radius of the nuclear disc from (Gadotti et al. 2020). The resulting fits are shown in Fig. 3 and the results summarised in Table 2. These measurements support the considera-

tions above and confirm that the radial profiles of metallicity and [α/Fe] are significantly flatter along the inner bar major axis, as compared to the minor axis profiles.

In Fig. 4, we compare the absolute values of the age and metallicity slopes along the inner bar major and minor axis with those obtained by Neumann et al. (2020) for main bars in different TIMER galaxies. The relative steepening/flattening of the age/metallicity profiles along the inner bar major axis – as compared to the minor axis – is well compatible with the results for main bars, as indicated by the systematic offset from the one-to-one correspondence line. The absolute values of the slopes of the inner bars may vary substantially from those of main bars but this is expected from the different assembly history of nuclear discs and main galaxy discs. In contrast to main discs, nuclear discs are formed through bar-driven processes (Bittner et al. 2020), hence the absolute age slope is set by the timescale of these processes. Similarly, a comparison of minor axis fits between inner and main bars is elusive, as those probe distinct structural components of the galaxies, that is nuclear discs and main discs.

Finally, we point out that the relative differences in the stellar population properties discussed above are of the same order of magnitude as the typical measurement errors presented in the literature (see e.g., Gadotti et al. 2019; Pinna et al. 2019; Bittner et al. 2020). However, while comparing absolute values of stellar population properties between different galaxies involves large uncertainties, this is not the case when considering trends within the same galaxy. In other words, it is unlikely that the observed systematic differences in the population content within one galaxy arise from random uncertainties in the measurement procedure, in particular since the trends presented in Fig. 3 are averaged over many spatial bins. In the right-hand panels of Fig. 3 we compare the distributions of stellar population properties along and perpendicular to the inner bar major axis within its radial range. For ages, metallicities, and [α/Fe] abundances of both galaxies, an Anderson-Darling test confirms at a 99.9% significance level that both observed distributions are not drawn from an identical parent distribution.

4. Discussion

In this section we discuss our findings on the stellar population properties of inner bars in comparison with analogous measurements in main bars. We further highlight these results in the context of the dynamical mechanisms of orbital age separation and orbital mixing. We remind the reader that the galaxies in the present sample exhibit high total stellar masses (see Table 1) and low-mass barred galaxies might follow trends different from those discussed in the following (see e.g., Elmegreen & Elmegreen 1985; Kruk et al. 2018; Zurita et al. 2020).

4.1. Stellar populations in bars, inner bars, and their star formation deserts

Main bars are not only detectable based on their morphology or kinematic features, but can also be identified by their stellar population content. In particular, bars typically exhibit higher metallicities and show lower [α/Fe] abundances, as compared to their immediate surroundings or the main disc (see e.g., Pérez et al. 2007, 2009; Sánchez-Blázquez et al. 2011, 2014; Fragkoudi et al. 2020; Neumann et al. 2020). While this finding does not necessarily hold true when comparing bars to the outer parts of the main galaxy disc (see e.g., Seidel et al. 2016), it does when bars are compared to the part of the disc within the

bar radius but outside of the bar itself, a region often denoted as 'star formation desert' (SFD; see e.g., James et al. 2009; James & Percival 2016; Donohoe-Keyes et al. 2019). Basically, these studies suggest that star formation in the SFD is suppressed very rapidly after bar formation. In contrast, star formation in the bar itself continues at least for a limited amount of time, although at relatively low rates, resulting in slightly younger stellar populations in the bar. Due to this continuing self-enrichment, the bar eventually reaches higher metallicities and depleted [α/Fe] enhancements, as compared to the SFD. Hence, the star formation desert can be identified as a region within the bar radius but outside of the bar itself that is characterised by relatively low metallicities and elevated [α/Fe] abundances.

Interestingly, in Sect. 3.1 we find similar results for the stellar population content of inner bars. In particular, inner bars exhibit elevated values of [M/H] and depleted [α/Fe] abundances, as compared to the region outside of the inner bar but within the inner bar radius (i.e. the star formation desert of the inner bar). Moreover, Fig. 3 indicates that inner bars are slightly younger along than perpendicular to their major axis. Nonetheless, previous findings (e.g., de Lorenzo-Cáceres et al. 2019) indicating that the inner bar of NGC 1291 is slightly older compared to its SFD suggest that, at least in some cases, star formation is suppressed more rapidly in the bar itself (see also Verley et al. 2007; Neumann et al. 2019, 2020; Fraser-McKelvie et al. 2020; Díaz-García et al. 2020).

In general, based on maps of the mean stellar population properties alone, bars and inner bars appear similar in terms of their relative population content. To date, inner bars were only marginally resolved in integral-field spectroscopic observations, due to the different spatial scales of main and inner bars. However, this limitation is now overcome by the high spatial sampling of the MUSE spectrograph. Visually comparing the inner bars in this study to the main bars observed in the TIMER survey (see Neumann et al. 2020), highlights the similarities of the stellar population content between bars and inner bars. In addition, a comparison of the properties of inner bars to the area within the inner bar radius but outside of the inner bar itself suggests the presence of a star formation desert related to inner bars, again as in main bars.

4.2. Flat population gradients along inner bars: Orbital mixing

Another relevant aspect when considering mean stellar population properties of bars are their gradients along the bar major axis, an aspect that holds information on their dynamical structure. More specifically, bars are elongated components which are built-up by a large number of elongated stellar orbits. These orbits might be composed of different stellar populations, show distinct levels of elongation, and reach different maximum radii in the bar. However, this does not only result in more elongated orbits dominating the spatial regions at the ends of the bars (see Sect. 4.3), but also causes different orbits to come very close to each other within the majority of the radial extent of the bar. In other words, stars on different orbits cross the same spatial region in the galaxy (see e.g., Binney & Tremaine 1987; Contopoulos & Grosbol 1989; Athanassoula 1992). Therefore, at each location in the bar the light contributions of different stellar populations on different orbits appear mixed and the gradients of the stellar population content in the main parts of the bars, in particular [M/H] and [α/Fe], are expected to be comparably flat.

In fact, recent observations suggest a flattening of the stellar populations gradients along the major axis of the bar, well

consistent with the theoretical considerations above (see e.g., Sánchez-Blázquez et al. 2011; Williams et al. 2012; Seidel et al. 2016; Fraser-McKelvie et al. 2019; Neumann et al. 2020). To date, radial population gradients could only be derived for main bars, as the spatial resolution remained a limiting factor.

In this study, we present for the first time radial gradients of the mean stellar population properties along both the inner bar major and minor axis. Similar to main bars, we find that the radial gradients of metallicities and [α/Fe] abundances along the inner bars major axis are significantly flatter compared to the profiles along the minor axis. This flattening resembles the stellar population profiles previously observed in main bars. This suggests that inner bars have a significant impact on the radial distribution of stellar populations in nuclear discs and hence that the orbital mixing which is evident in bars occurs in inner bars as well. Again, this result reinforces the idea that inner bars are dynamically distinct components that form and evolve in the same way main bars do.

Interestingly, while a flattening of the radial gradients along the inner bar major axis is prominent for metallicities and [α/Fe] abundances, no such gradient is evident in the stellar age profiles. Instead, the measured stellar ages typically decrease from the centre of the galaxy to the outer edge of the nuclear disc. In fact, such negative gradients in age are frequently observed in nuclear discs, regardless of the presence of an inner bar, and appear to be a result of their inside-out formation scenario (Bittner et al. 2020). In addition, orbital age separation, that is the dynamical effect that the ends of bars are younger than their central parts, should also hinder the development of flat age profiles. We detail this aspect in the following subsection.

4.3. Young ends of inner bars: Orbital age separation

Main bars do not only appear distinguished from their surroundings by their elevated metallicities and depleted [α/Fe] abundances, but also show spatially well-defined variations in age. The ends of main bars generally appear significantly younger compared to the rest of the bar. While this effect could be a result of enhanced star formation in these regions, the inspection of Hα emission-line maps has shown that no signatures of ongoing star formation are detected. Instead, this observation is a result of orbital age separation (also referred to as kinematic fractionation) and known from both observational and numerical studies on the stellar population content of bars (see e.g., Pérez et al. 2007; Wozniak 2007; Fragkoudi et al. 2017, 2018; Athanassoula et al. 2017; Debattista et al. 2017; Neumann et al. 2020).

These studies find that distinct kinematic components of the galaxy disc participate in bars in different ways. Kinematically cold stars (i.e. those with a low radial velocity dispersion) preferably end up in highly elongated x_1 orbits (oriented along the bar major axis) while kinematically hot stars (i.e. those with high radial velocity dispersion) form rounder and less elongated bar x_1 orbits. Since more elongated orbits extend to larger radii, the ends of the bars are dominated by stars on the most elongated orbits. In the main disc of a typical galaxy, these kinematically cold and hot components could be the thin and thick disc (Fragkoudi et al. 2017; Debattista et al. 2017; Athanassoula et al. 2017). While the thick disc is typically thought to be old, metal-poor, and shows high velocity dispersions, the thin disc is younger, more metal-rich, and exhibits low velocity dispersions (see e.g., Prochaska et al. 2000; Cheng et al. 2012; Pinna et al. 2019). As a consequence of this, the young stars of the thin disc end up on more elongated bar orbits and thus dominate the spatial region at the ends of the bar, hence creat-

ing the effect that the ends of bars show younger stellar populations. Interestingly, this effect is most prominent for stellar ages, but absent when considering metallicities and [α/Fe] abundances, in contrast to the simulations of Fragkoudi et al. (2018). A possible explanation could be that age is a better tracer of the stellar kinematics, or, more precisely, of the velocity dispersion (see e.g., Peletier et al. 2007; Falcón-Barroso 2016). The longer a stellar population was present in the disc of a galaxy, the longer it was exposed to dynamical heating processes, resulting in an increased velocity dispersion. Hence, the velocity dispersion should be a function of stellar age and, therefore, the ends of bars can be observed to exhibit younger stellar populations. In contrast, stars of a given age can have a range of metallicities and [α/Fe] enhancements, so that these quantities are not necessarily a function of stellar velocity dispersion, and therefore the ends of bars and inner bars do not necessarily show distinct [M/H] and [α/Fe] values.

In all galaxies in this study, we do detect such younger stellar populations in a spatially confined region at the ends of the inner bars. As a result, these relatively young ends spatially coincide with σ-hollows in these galaxies (de Lorenzo-Cáceres et al. 2019; Méndez-Abreu et al. 2019; Bittner et al. 2019). These regions of significantly lower stellar velocity dispersion are typically detected towards the ends of inner bars, that is in areas in which the inner bar dominates the stellar light (de Lorenzo-Cáceres et al. 2008, 2013). Observing younger stellar populations in the same regions hints towards the existence of the dynamical effect of orbital age separation in inner bars. This again suggests that inner bars work dynamically identical to bars, differing only in the spatial scale on which they form from disc instabilities.

This result also indicates that stars from kinematically different components participate in the inner bar. Analogous to the main bar existing in both the thick and thin main disc, one might speculate if nuclear discs consist of hotter and colder nuclear disc components as well or that the hot main disc component might participate in the inner bar. However, dedicated studies, in particular numerical simulations of nuclear disc formation in a self-consistent cosmological context, are necessary to shed further light on these aspects.

Finally, a frequent photometric feature of strong bars in early-type spirals are surface brightness enhancements at their ends, a structure typically referred to as ansae (Martinez-Valpuesta et al. 2007; Buta et al. 2015). To date, these structures have not been studied intensively and their physical origin as well as presence in inner bars remains elusive. Here we speculate that the systematically younger stellar populations at the ends of inner and main bars could be connected to photometric ansae. In fact, these younger stellar populations, in particular in the case of NGC 1291, resemble the morphological appearance of ansae in photometric studies. Such younger stellar populations are expected to be relatively brighter and (at a given surface mass density) should result in elevated surface brightnesses. Other mechanisms, such as enhanced star formation at the ends of bars, or the dynamical trapping of stars around the ansae (Martinez-Valpuesta et al. 2007), might as well contribute to this phenomenon.

5. Summary and conclusions

We have exploited MUSE observations of the central regions of the three galaxies NGC 1291, NGC 1433, and NGC 5850, observed as part of the TIMER survey. All galaxies clearly exhibit nuclear discs, and two of them host prominent inner bars.

The inner bar in NGC 1433 appears weaker and less elongated particularly in earlier imaging data, but is clearly detected in our new, AO-assisted, H-band photometric observations. In the present study, we have used the full spectral fitting code pPXF in order to derive spatially resolved maps and radial profiles of the mean stellar population properties in the inner bars. We compare these results to those obtained for main bars, and further use them to constrain their dynamical structure. Our main results are as follows:

(i) Inner bars can be clearly distinguished, based on their mean stellar population properties alone. In particular, they are characterised by elevated metallicities and depleted [α/Fe] abundances, as compared to the region outside of the inner bar but within the inner bar radius. Although inner bars show systematically younger ages, these differences are generally small. Based on spatially resolved, high-resolution maps of the mean population properties and their relative values, inner and main bars appear identical.

(ii) Radial profiles of metallicities and [α/Fe] abundances along the inner bar major axis are flat, while minor axis profiles exhibit steeper slopes. This observational effect of radial mixing is known from main bars, and suggests that inner bars significantly affect the distribution of stars in the nuclear discs. This effect is consistent with inner bars being built by stars on strongly elongated orbits, analogous to the x_1 orbits in main bars.

(iii) The ends of the inner bars exhibit younger mean ages, as compared to the rest of the inner bars. This effect is known from main bars as kinematic fractionation or orbital age separation and suggests that the youngest stars, that is those with the lowest radial velocity dispersion, occupy the most elongated x_1 orbits. This effect might as well explain the formation of σ-hollows at the ends of the inner bars.

(iv) We speculate that the observed young ends of bars and inner bars could be one possible mechanism to create the morphological feature of ansae, in particular as younger stellar populations have a higher surface brightness at a given stellar mass surface density.

The above results, in particular orbital mixing and orbital age separation, together with results from de Lorenzo-Cáceres et al. (2019) and Méndez-Abreu et al. (2019) reinforce the idea that barred galaxies can be rather like Babushka dolls, in which we have a 'galaxy within a galaxy': inner bars appear to be dynamically very similar to the main bars of disc galaxies. The main difference between these galaxy components is the spatial scale on which they form and evolve.

Astronomy (Astropy Collaboration 2013, 2018); NumPy Oliphant (2006); SciPy (Virtanen et al. 2020); and Matplotlib (Hunter 2007).

References

Aguerri, J. A. L., Méndez-Abreu, J., & Corsini, E. M. 2009, A&A, 495, 491
Astropy Collaboration (Robitaille, T. P., et al.) 2013, A&A, 558, A33
Astropy Collaboration (Price-Whelan, A. M., et al.) 2018, AJ, 156, 123
Athanassoula, E. 1992, MNRAS, 259, 328
Athanassoula, E., Lambert, J. C., & Dehnen, W. 2005, MNRAS, 363, 496
Athanassoula, E., Rodionov, S. A., & Prantzos, N. 2017, MNRAS, 467, L46
Bacon, R., Copin, Y., Monnet, G., et al. 2001, MNRAS, 326, 23
Bacon, R., Accardo, M., Adjali, L., et al. 2010, in The MUSE Second-generation VLT Instrument, SPIE Conf. Ser., 7735, 773508
Bacon, R., Conseil, S., Mary, D., et al. 2017, A&A, 608, A1
Barazza, F. D., Jogee, S., & Marinova, I. 2008, ApJ, 675, 1194
Binney, J., & Tremaine, S. 1987, Galactic Dynamics (Princeton: Princeton University Press)
Bittner, A., Falcón-Barroso, J., Nedelchev, B., et al. 2019, A&A, 628, A117
Bittner, A., Sánchez-Blázquez, P., Gadotti, D. A., et al. 2020, A&A, 643, A65
Bundy, K., Bershady, M. A., Law, D. R., et al. 2015, ApJ, 798, 7
Bureau, M., & Athanassoula, E. 2005, ApJ, 626, 159
Buta, R. 1986, ApJS, 61, 631
Buta, R. J., Sheth, K., Athanassoula, E., et al. 2015, ApJS, 217, 32
Cappellari, M. 2017, MNRAS, 466, 798
Cappellari, M., & Copin, Y. 2003, MNRAS, 342, 345
Cappellari, M., & Emsellem, E. 2004, PASP, 116, 138
Cheng, J. Y., Rockosi, C. M., Morrison, H. L., et al. 2012, ApJ, 752, 51
Contopoulos, G., & Grosbol, P. 1989, A&ARv, 1, 261
de Lorenzo-Cáceres, A., Falcón-Barroso, J., Vazdekis, A., & Martínez-Valpuesta, I. 2008, ApJ, 684, L83
de Lorenzo-Cáceres, A., Vazdekis, A., Aguerri, J. A. L., Corsini, E. M., & Debattista, V. P. 2012, MNRAS, 420, 1092
de Lorenzo-Cáceres, A., Falcón-Barroso, J., & Vazdekis, A. 2013, MNRAS, 431, 2397
de Lorenzo-Cáceres, A., Sánchez-Blázquez, P., Méndez-Abreu, J., et al. 2019, MNRAS, 484, 5296
de Lorenzo-Cáceres, A., Méndez-Abreu, J., Thorne, B., & Costantin, L. 2020, MNRAS, 494, 1826
de Vaucouleurs, G. 1974, in The Formation and Dynamics of Galaxies, ed. J. R. Shakeshaft, IAU Symp., 58, 335
de Vaucouleurs, G. 1975, ApJS, 29, 193
Debattista, V. P., Carollo, C. M., Mayer, L., & Moore, B. 2005, ApJ, 628, 678
Debattista, V. P., Ness, M., Gonzalez, O. A., et al. 2017, MNRAS, 469, 1587
Díaz-García, S., Moyano, F. D., Comerón, S., et al. 2020, A&A, 644, A38
Donohoe-Keyes, C. E., Martig, M., James, P. A., & Kraljic, K. 2019, MNRAS, 489, 4992
Elmegreen, B. G., & Elmegreen, D. M. 1985, ApJ, 288, 438
Erwin, P. 2004, A&A, 415, 941
Erwin, P., & Sparke, L. S. 2002, AJ, 124, 65
Falcón-Barroso, J. 2016, in The Stellar Kinematics of Extragalactic Bulges, eds. E. Laurikainen, R. Peletier, & D. Gadotti, Astrophys. Space Sci. Lib., 418, 161
Falcón-Barroso, J., Bacon, R., Bureau, M., et al. 2006, MNRAS, 369, 529
Falcón-Barroso, J., Sánchez-Blázquez, P., Vazdekis, A., et al. 2011, A&A, 532, A95
Fragkoudi, F., Di Matteo, P., Haywood, M., et al. 2017, A&A, 606, A47
Fragkoudi, F., Di Matteo, P., Haywood, M., et al. 2018, A&A, 616, A180
Fragkoudi, F., Grand, R. J. J., Pakmor, R., et al. 2020, MNRAS, 494, 5936
Fraser-McKelvie, A., Merrifield, M., Aragón-Salamanca, A., et al. 2019, MNRAS, 488, L6
Fraser-McKelvie, A., Aragón-Salamanca, A., Merrifield, M., et al. 2020, MNRAS, 495, 4158
Gadotti, D. A. 2008, MNRAS, 384, 420
Gadotti, D. A. 2011, MNRAS, 415, 3308
Gadotti, D. A., Sánchez-Blázquez, P., Falcón-Barroso, J., et al. 2019, MNRAS, 482, 506
Gadotti, D. A., Bittner, A., Falcón-Barroso, J., et al. 2020, A&A, 643, A14
Gonçalves, G., Coelho, P., Schiavon, R., & Usher, C. 2020, MNRAS, 499, 2327
Herrera-Endoqui, M., Díaz-García, S., Laurikainen, E., & Salo, H. 2015, A&A, 582, A86
Hildebrandt, A., de Lorenzo-Cáceres, A., Méndez-Abreu, J., & Falcón-Barroso, J. 2020, MNRAS, submitted

Hunter, J. D. 2007, Comput. Sci. Eng., 9, 90
Iannuzzi, F., & Athanassoula, E. 2015, MNRAS, 450, 2514
James, P. A., & Percival, S. M. 2016, MNRAS, 457, 917
James, P. A., Bretherton, C. F., & Knapen, J. H. 2009, A&A, 501, 207
Jungwiert, B., Combes, F., & Axon, D. J. 1997, A&AS, 125, 479
Kissler-Patig, M., Pirard, J. F., Casali, M., et al. 2008, A&A, 491, 941
Kormendy, J., & Kennicutt, R. C., Jr. 2004, ARA&A, 42, 603
Kraljic, K., Bournaud, F., & Martig, M. 2012, ApJ, 757, 60
Kroupa, P. 2001, MNRAS, 322, 231
Kruk, S. J., Lintott, C. J., Bamford, S. P., et al. 2018, MNRAS, 473, 4731
Laine, S., Shlosman, I., Knapen, J. H., & Peletier, R. F. 2002, ApJ, 567, 97
Li, Z.-Y., Shen, J., Bureau, M., et al. 2018, ApJ, 854, 65
Martinez-Valpuesta, I., Knapen, J. H., & Buta, R. 2007, AJ, 134, 1863
Masters, K. L., Nichol, R. C., Hoyle, B., et al. 2011, MNRAS, 411, 2026
McDermid, R. M., Alatalo, K., Blitz, L., et al. 2015, MNRAS, 448, 3484
Méndez-Abreu, J., Corsini, E. M., Debattista, V. P., et al. 2008, ApJ, 679, L73
Méndez-Abreu, J., Debattista, V. P., Corsini, E. M., & Aguerri, J. A. L. 2014, A&A, 572, A25
Méndez-Abreu, J., de Lorenzo-Cáceres, A., Gadotti, D. A., et al. 2019, MNRAS, 482, L118
Muñoz-Mateos, J. C., Sheth, K., Gil de Paz, A., et al. 2013, ApJ, 771, 59
Muñoz-Mateos, J. C., Sheth, K., Regan, M., et al. 2015, ApJS, 219, 3
Neumann, J., Gadotti, D. A., Wisotzki, L., et al. 2019, A&A, 627, A26
Neumann, J., Fragkoudi, F., Pérez, I., et al. 2020, A&A, 637, A56
Ocvirk, P., Pichon, C., Lançon, A., & Thiébaut, E. 2006a, MNRAS, 365, 74
Ocvirk, P., Pichon, C., Lançon, A., & Thiébaut, E. 2006b, MNRAS, 365, 46
Oliphant, T. E. 2006, A Guide to NumPy (USA: Trelgol Publishing), 1
Paufique, J., Bruton, A., Glindemann, A., et al. 2010, in Adaptive Optics Systems II, eds. B. L. Ellerbroek, M. Hart, N. Hubin, & P. L. Wizinowich, SPIE Conf. Ser., 7736, 77361P
Peletier, R. F., Falcón-Barroso, J., Bacon, R., et al. 2007, MNRAS, 379, 445
Pérez, I., Sánchez-Blázquez, P., & Zurita, A. 2007, A&A, 465, L9
Pérez, I., Sánchez-Blázquez, P., & Zurita, A. 2009, A&A, 495, 775
Pietrinferni, A., Cassisi, S., Salaris, M., & Castelli, F. 2004, ApJ, 612, 168
Pietrinferni, A., Cassisi, S., Salaris, M., & Castelli, F. 2006, ApJ, 642, 797
Pietrinferni, A., Cassisi, S., Salaris, M., Percival, S., & Ferguson, J. W. 2009, ApJ, 697, 275
Pietrinferni, A., Cassisi, S., Salaris, M., & Hidalgo, S. 2013, A&A, 558, A46
Pinna, F., Falcón-Barroso, J., Martig, M., et al. 2019, A&A, 623, A19
Press, W. H., Teukolsky, S. A., Vetterling, W. T., & Flannery, B. P. 1992, Numerical Recipes in FORTRAN. The Art of Scientific Computing (Cambridge: Cambridge University Press)
Prochaska, J. X., Naumov, S. O., Carney, B. W., McWilliam, A., & Wolfe, A. M. 2000, AJ, 120, 2513
Sánchez, S. F., Kennicutt, R. C., Gil de Paz, A., et al. 2012, A&A, 538, A8
Sánchez-Blázquez, P., Ocvirk, P., Gibson, B. K., Pérez, I., & Peletier, R. F. 2011, MNRAS, 415, 709
Sánchez-Blázquez, P., Rosales-Ortega, F. F., Méndez-Abreu, J., et al. 2014, A&A, 570, A6
Sarzi, M., Falcón-Barroso, J., Davies, R. L., et al. 2006, MNRAS, 366, 1151
Seidel, M. K., Falcón-Barroso, J., Martínez-Valpuesta, I., et al. 2016, MNRAS, 460, 3784
Sheth, K., Elmegreen, D. M., Elmegreen, B. G., et al. 2008, ApJ, 675, 1141
Sheth, K., Regan, M., Hinz, J. L., et al. 2010, PASP, 122, 1397
Shlosman, I., Frank, J., & Begelman, M. C. 1989, Nature, 338, 45
Shlosman, I., Begelman, M. C., & Frank, J. 1990, Nature, 345, 679
Vazdekis, A., Coelho, P., Cassisi, S., et al. 2015, MNRAS, 449, 1177
Verley, S., Combes, F., Verdes-Montenegro, L., Bergond, G., & Leon, S. 2007, A&A, 474, 43
Virtanen, P., Gommers, R., Oliphant, T. E., et al. 2020, Nat. Meth., 17, 261
Weilbacher, P. M., Streicher, O., Urrutia, T., et al. 2012, in Design and Capabilities of the MUSE Data Reduction Software and Pipeline, SPIE Conf. Ser., 8451, 84510B
Weilbacher, P. M., Palsa, R., Streicher, O., et al. 2020, A&A, 641, A28
Weiss, A., Peletier, R. F., & Matteucci, F. 1995, A&A, 296, 73
Wenger, M., Ochsenbein, F., Egret, D., et al. 2000, A&AS, 143, 9
Williams, M. J., Bureau, M., & Kuntschner, H. 2012, MNRAS, 427, L99
Worthey, G., Faber, S. M., & Gonzalez, J. J. 1992, ApJ, 398, 69
Wozniak, H. 2007, A&A, 465, L1
Zurita, A., Florido, E., Bresolin, F., Pérez, I., & Pérez-Montero, E. 2020, MNRAS, 500, 2380